We are IntechOpen,
the world's leading publisher of
Open Access books
Built by scientists, for scientists

6,900
Open access books available

185,000
International authors and editors

200M
Downloads

154
Countries delivered to

Our authors are among the

TOP 1%
most cited scientists

12.2%
Contributors from top 500 universities

CLARIVATE ANALYTICS
BOOK CITATION INDEX
INDEXED

WEB OF SCIENCE™

Selection of our books indexed in the Book Citation Index
in Web of Science™ Core Collection (BKCI)

Interested in publishing with us?
Contact book.department@intechopen.com

Numbers displayed above are based on latest data collected.
For more information visit www.intechopen.com

Preparation of transparent conductive AZO thin films for solar cells

Vladimir Tvarozek[1], Pavol Sutta[2], Sona Flickyngerova[1], Ivan Novotny[1],
Pavol Gaspierik[1], Marie Netrvalova[2] and Erik Vavrinsky[1]
[1]Department of Microelectronics, Slovak University of Technology in Bratislava
[2]Department of Materials & Technology, West Bohemian University, Plzen
[1]Slovakia, [2]Czech Republic

1. Introduction

Transparent conducting oxides (TCOs) based on ZnO are promising for application in thin-film solar photovoltaic cells (PVCs) and various optoelectronic devices (Minami, 2005). Desired parameters of ZnO and doped ZnO:Al (AZO) thin films are given by their role in superstrate configuration of tandem Si solar cell (Zeman, 2007): the light enters the cell through the glass substrate where two pin absorber thin-film structures are placed between two TCO layers with back metal contact. The upper front contact AZO layer should fulfill several important requirements: high transparency in VIS/near IR solar spectrum; high electrical conductivity; suitable surface texture in order to enhance light scattering and absorption inside the cell; high chemical stability and adhesion to silicon. Moreover, bottom ZnO interlayer between Si and metal (usually Ag) contact is acting as barier and adhesion layer as well as optical matching layer to Ag back contact to improve its reflection of radiation, particularly in near IR region (Dadamseh et al., 2008). Optimization of the front contact TCO has proven to be crucial for getting the high cell efficiency (Berginski et al., 2008).

RF sputtering is owning several advantages in comparison with the other physical and chemical deposition methods: a low-temperature ion–assisted deposition of metals, semiconductors, insulators, the before/post deposition modification of substrate/thin - film surface by ions on the micro-/nano- level; change of deposition rate in wide range (0,1 to 10 nm/s); to control further parameters which are important for thin film growth (substrate temperature, plasma density, composition of working gas, ion bombardment of film during deposition). In addition there is a significant contribution of secondary electron bombardment to the atomic scale heating of the film when it is prepared by the RF diode sputtering.

Therefore RF sputtering of AZO films from ceramic target is often used to get the best their electrical and optical properties. An influence of different technological parameters was investigated: partial pressure of oxygen (Tsui & Hirohashi, 2000), substrate temperature (Fu & Zhuang, 2004), (Ali, 2006), (Berginski et al., 2008), substrate bias voltage (Ma & Hao, 2002), (Lim & Kim, 2006), post-deposition annealing (Fang at al., 2002), (Oh et al., 2007), (Berginski

et al., 2008), surface-texturing by chemical etching (Kluth & Rech, 1999), (Berginski et al., 2008) or ion-sputter etching (Flickyngerova, et al. 2009). The complex study and an optimization of various deposition parameters were done by using in-line AC magnetron sputtering system with Zn/Al compound targets (Sittinger et al., 2006).

In general, sputter deposition is determined by complex processes proceeded: (a) at the target bombarded by energetic ions, (b) in the low-temperature plasma, (c) on the surface of substrate and growing film. In general, thin film growth is influenced by the kinetic energy of coating species on the substrate – in addition to substrate temperature a total energy flux is acting to the substrate and growing thin film. It depends mainly on the amount and the energy of: (i) sputtered coating species, (ii) energetic neutral working gas atoms (neutralized and reflected at the target), (iii) energetic secondary electrons emitted from the target, (iv) negative ions coming from the working gas plasma or target, (v) ions bombarding the substrate in bias or reactive mode. These effects can cause significant changes in the crystallic structure, surface morphology and chemical stoichiometry of sputtered thin films, i.e. they can modify their electrical and optical properties. The existence of high-energy particles bombarding the film during both the planar diode and the planar magnetron sputtering of ZnO was confirmed (Tominaga et al., 1982). It was found from energy analyses that the high-energy neutral oxygen atoms should be taken into account above working pressures 1.3 Pa and negative oxygen ions accelerated at the target becomes important at pressures in the range of 0.1 Pa. The negative ion resputtering by oxygen ions during sputtering of ZnO:Al thin films has caused extended defects in the film crystalline structure (interstitials, lattice expansion, grain boundaries) - it was responsible for the degradation of electrical properties of these films (Kluth et al., 2003), (Rieth & Holloway, 2004). Thornton's microstructural model developed for sputtered metal thin films (Thorton & Hoffman, 1989) they modified for magnetron sputtered ZnO at low-/medium-/high-pressure regions (0.04 - 4 Pa) and they discussed the correlation of sputter parameters (sputter gas pressure and substrate temperature) to structural and electrical properties of thin film. These results and next ones obtained also later (Kluth et al., 2006) showed a strong dependence of ZnO:Al thin film properties on sputter gas pressure and oxygen content in working gas.

Structural models based on Thornton's assumptions are well satisfied in the technological approach of sputtering of metals. In the parameter „Ar working gas pressure" he implicitly included collisions between the sputtered and Ar atoms at elevated pressures causing the deposited atoms to arrive at the substrate in randomized directions that promote oblique coating. Therefore to use more physical approach, in addition to substrate temperature Ts, we introduced a total energy flux density E_Φ [W/m^2] affecting to the substrate and the growing thin film (Fig. 1). A total energy flux density, by other words power density E_Φ, can be expressed by microscopic quantities known from the kinetic theory of gases, low-temperature plasma physics and the models of sputtering processes. It can be also estimated by macroscopic sputtering parameters like supply RF power, deposition rate, average DC voltage induced on target, flow or pressure of working gases, substrate bias voltage or power (Tvarozek et al., 2007). The substrate temperature is normalized to the melting temperature T_m of sputtered material, T_s/T_m. The substrate temperatures are usually very far from melting point of ZnO (T_m = 1975°C) during the sputtering that's why we found useful to express T_s/T_m in logarithmic scale. The ratio of the total energy flux density E_Φ and its minimum value $E_{\Phi min}$ specified by the sputtering mode and the geometrical arrangement of the sputtering system is $E_\Phi/E_{\Phi min}$. Optimal conditions for deposition of

semiconductor oxides and nitrides (ITO, TiN, ZnO, ZnO:N, ZnO:Al, ZnO:Ga, ZnO:Sc) in our diode sputtering system corresponded to the relative total energy flux density E_Φ / $E_{\Phi min}$ in the range of $4 \div 7$, $E_{\Phi min} \sim 1 \times 10^4 \, W/m^2$, (Fig. 1, dashed lines).
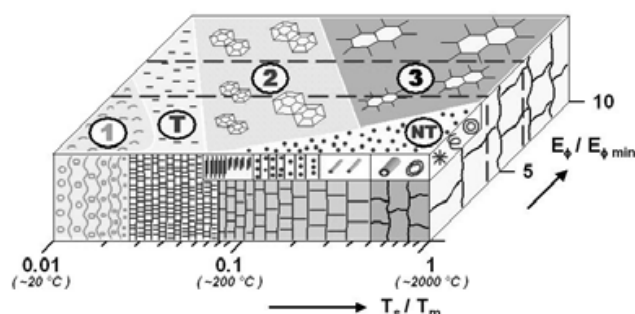

Fig. 1. Crystalline structure zone model of sputtered ZnO thin films: Zone 1 – porous structure of tapered amorphous or crystalline nanograins separated by voids, Zone T – dense polycrystalline structure of fibrous and nanocrystalline grains, Zone 2 – columnar grain structure, Zone 3 – single-crystal micrograin structure, Zone NT – nanostructures and nanoelements.

The aim of present work has been to find correlations among the technological parameters (power density, substrate temperature and post-deposition annealing) and structural / electrical / optical properties of AZO thin films. In the beginning to accelerate our investigation of desirable thin film properties we used the RF diode sputtering where one can get continual changes of thin film thickness (of composition also) in one deposition run.

2. Modelling and simulation

Computer simulations have proved to be an indispensable tool for obtaining a better understanding of solar photovoltaic cells (PVC) performance and for determining trends for optimizing material parameters and solar cell structures. We focused on the simulations of both the parasitic effect in real bulk PVCs and progressive thin film solar PVCs, based on amorphous silicon and transparent conductive layers of ZnO, ZnO:Al.
Sputtering is an important technique for deposition of both multicomponent thin films for solar applications as well as multilayer coatings with only few nanometers thin layers (so-called superlattices) which exhibit superior hardness, high wear, corrosion resistance and thermal stability (Panjan, 2007). Sputter deposition is attractive particularly in industrial applications due to the need of high deposition rates and uniform coverage over large areas. Therefore it is desirable to know what influence has the sputter system arrangement on spatial distribution of sputtered particles on the top of substrate (so-called deposition profile), i.e. on homogeneity of growing film properties.

2.1 Electric properties of PVC
The most important electric parameters, which are used to characterize the quality of PVC, are defined: the short-circuit current I_{SC} (the current through the solar cell when the voltage

across the solar cell is zero), the open-circuit voltage V_{OC} (the maximum voltage available from a solar cell, at zero current), the fill factor FF (indicating how far the product $I_{SC}V_{OC}$ is from the power delivered by the PVC) and the conversion efficiency (η).

The conversion efficiency is defined as the ratio of the photovoltaically generated electric output of the cell to the radiation power falling on it P_{in}:

$$\eta = \frac{I_m V_m}{P_{in}} = FF \frac{I_{SC}V_{OC}}{E \times A} = FF \frac{J_{SC}V_{OC}}{E} , \qquad (1)$$

where FF is the fill factor of PVC $I_m V_m / I_{SC} V_{OC}$ (or area ratio A / B in Fig. 2), E is value of irradiance and J_{SC} is the short-circuit current density I_{SC}/A. The values of V_m and I_m are the co-ordinates for maximal power point (he designates the optimal operating point of PVC), and can be estimated from the open circuit voltage and short circuit current: $V_m \sim (0.75\text{-}0.9) \times V_{OC}$, $I_m \sim (0.85\text{-}0.95) \times I_{SC}$ (Goetzberger & Hoffmann, 2005). Efficiency is measured under standard test conditions (temperature of PVC 25°C, irradiance 1000 Wm^{-2}, air mass 1.5).
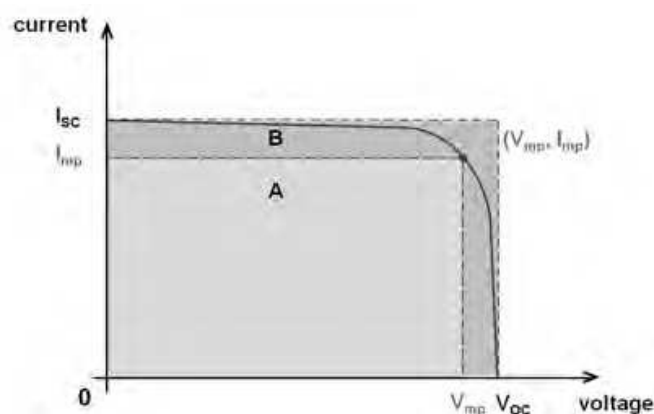

Fig. 2. C-V and P-V (dash line) characteristics of illuminated solar cell

2.2 PSPICE model of bulk solar cell the 1st generation

The model of simple 1st generation PVC (i.e. *p-n* junction represented as bulk silicon diode of large-area), following equivalent circuit diagram (Fig. 3) by PSpice software (PSpice A/D Circuit Simulator, 2009) for analysis of electronic circuits and their simulations, was created. By means of the two-diode model we achieved the better description of PVC. Diode D$_1$ is representing the carrier injection current I_{INJ} and diode D$_2$ the recombination current I_R. The values of saturation current densities and ideality factors for this diodes are different: J_{s1} = 1e-12 Acm^{-2}, J_{s2} = 1e-8 Acm^{-2}, m_1 = 1 (ideal diode), m_2 = 2. We define the size of PVC area A = 100 cm^2. The other components are of resistive nature, a parallel (or shunt) resistance R$_P$ and the series resistance R$_S$.

For obtaining high efficiency of PVC, the parallel parasitic resistance R$_P$ (described loss currents at the edges of the solar cell and surface inhomogeneities) should be as high as possible and the series resistance R$_S$ (the resistance through the wafer, the resistance of the back surface contact and the contact grid on the front surface) as a low as possible, ideally it's a deal: $R_S = 0$, $R_P \rightarrow \infty$. The values of parasitic resistances depend on PVC size, consequently also from area.
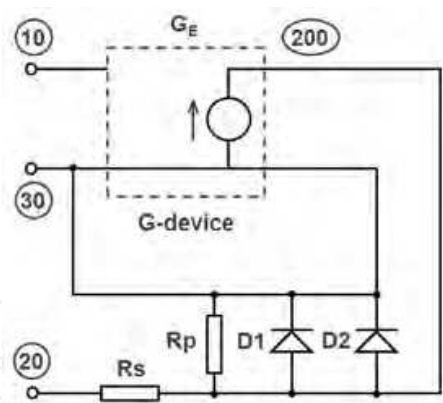
Fig. 3. Equivalent circuit of real bulk PVC modelled in PSpice

In PSpice is the value of the short circuit current I_{SC} assigned to a voltage-controlled current source (G-device, Fig.2) and is given by:

$$G_E = \frac{J_{SC}A}{1000}E \qquad (2)$$

We considered that the value of short-circuit current density J_{SC} is given at standard test conditions.

The effect of parasitic resistances R_S and R_P on C-V characteristic is shown in the Fig.4.

As can be seen, for parasitic serial resistance R_S (Fig.4a) the values of the short-circuit current and of the fill factor (it follows too efficiency) can be expressively reduced. At the high values of R_S occur the big reduction of the short-circuit current value I_{SC}. The open-circuit voltage is independent of the series resistance. The product $R_S.I_{SC}$ should never have been greater than 25 mV in praxis (outside temperature 25 °C).

The parallel resistance also degrades the performance of the PVC, Fig.4b.
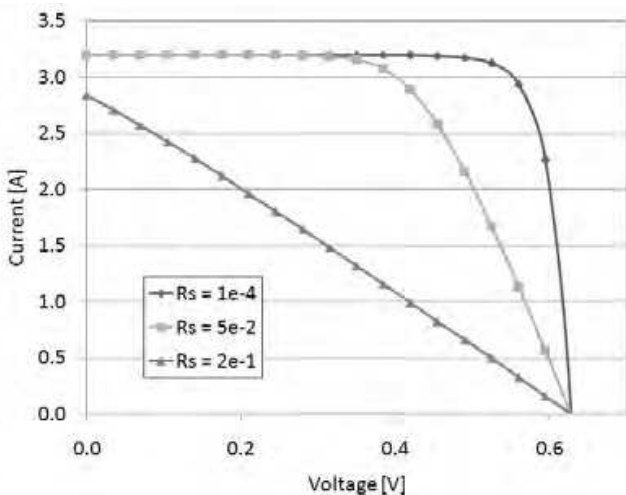
a)
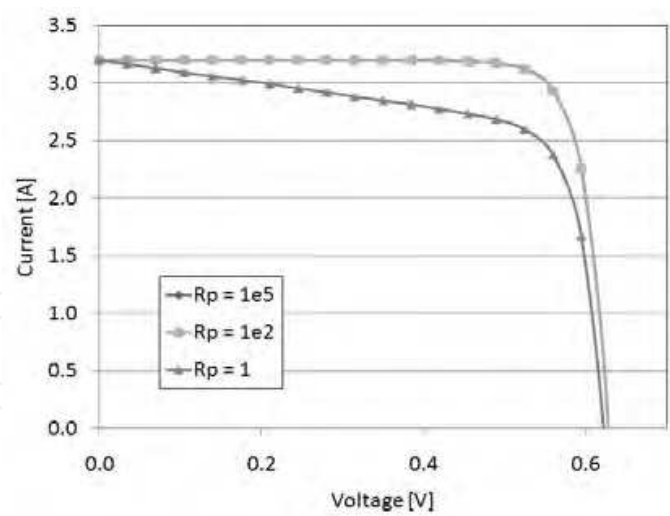
b)

Fig. 4. C-V characteristics of bulk PVC structure (illumination for AM1.5) for modification of serial (a) and parallel resistance (b)

Small values of the parallel resistance heavily degrade the fill factor (i.e. efficiency). Also are the value of open-circuit voltage reduced, the short-circuit current is independent of the parallel resistance.

The concrete values of parasitic resistances, that we used by the simulation with PSpice are:
- serial parasitic resistance R_S: 1e-4, 5e-2, 2e-1 Ω,
- parallel parasitic resistance R_P: 1e5, 1e2, 1 Ω.

Selected parameters of illuminated PVC with the parasitic resistances R_S and R_P is shown in the Tab.1. The parameters I_{SC} and V_{OC} are assigned from the graph, parameters FF and η are calculated by (eq. 1).

R_S (Ω)	I_{SC} (A)	V_{OC} (V)	FF (-)	η (%)
1e-4	3.200	0.628	0.825	16.58
5e-2	3.200	0.628	0.604	12.14
2e-1	2.844	0.628	0.261	4.66
R_P (Ω)	I_{SC} (A)	V_{OC} (V)	FF (-)	η (%)
1e5	3.2	0.628	0.825	16.58
1e2	3.2	0.628	0.824	16.56
1	3.2	0.622	0.686	13.65

Table 1. Selected parameters of bulk PVC structure (illumination for AM1.5)

2.3 ASA model of thin film solar cell the 2nd generation

Progressive solar PVC, 2nd and 3rd generation with higher efficiency of 20÷40%, are formed in thin film structures, predominantly based on amorphous silicon (a-Si:H, *p-i-n* junction) as the absorber material and transparent conducting oxide (TCO) semiconductors for transparent electrodes, e.g. single junction *p-i-n* a-Si PVC structure "glass/TCO/a-Si:H (*p-i-n*)/TCO/Ag or Al (reflective back contact)" or tandem solar cell structure

"glass/TCO/a-Si:H (*p-i-n*)/µc-Si:H (*p-i-n*)/ TCO/Ag or Al (reflective back contact)" (Zeman, 2007). For the simulation of the thin film PVC we have used the ASA program, developed at Delft University of Technology (Zeman et al., 2005), which is designed for the simulation of multilayered heterojunction device structures.
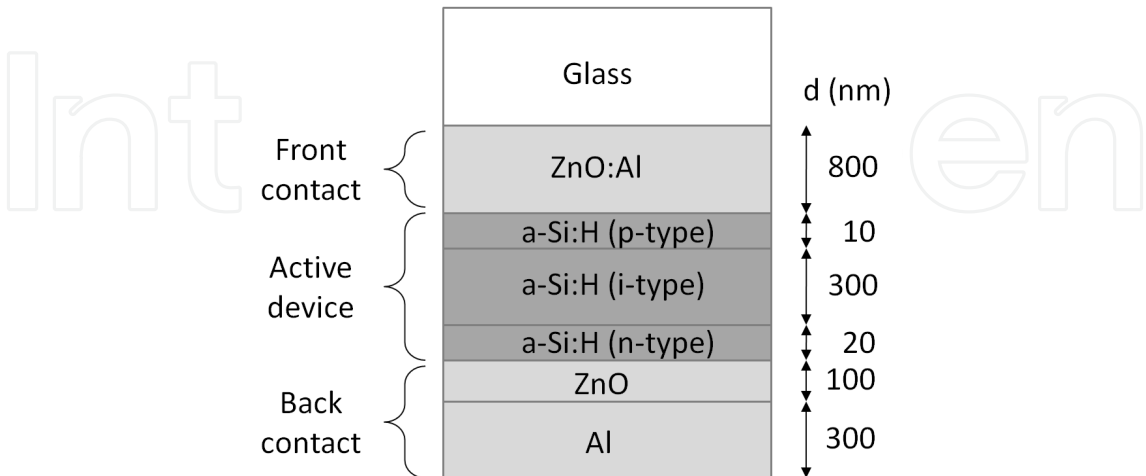

Fig. 5. Superstrate PVC configuration of single junction (*p-i-n*) structure

We focused for "superstrate" configuration of thin-film solar PVC: Glass/ZnO:Al/a-Si:H (*p-i-n*)/ZnO/Al (reflective back contact). Schematic structure of a single junction a-Si:H PVC is shown in Fig. 5. The active device consists of three layers: a *p*-type a-Si:H layer, an intrinsic a-Si:H layer and an n type a-Si:H layer. This layers form a *p-i-n* single junction. The doped layers set up an internal electric field across the intrinsic a-Si:H layer and establish low loss ohmic electrical contacts between the a-Si:H part of the PVC and the external electrodes (Zeman, 2007).

The thickness of the *i*-region should be optimized for maximum current generation. In practice is limit the *i*-region thickness to around 0.5 µm (Nelson, 2003).

Transparent conducting oxides based on ZnO are promising for application in thin-film solar photovoltaic cells. The upper front contact Zno:Al layer should fulfil several important requirements: high transparency in VIS/near IR solar spectrum; high electrical conductivity; suitable surface texture in order to enhance light scattering and absorption inside the cell; high chemical stability and adhesion to silicon. Moreover, bottom ZnO interlayer between Si and metal (usually Ag) contact is acting as barier and adhesion layer as well as optical matching layer to Ag back contact to improve its reflection of radiation, particularly in near IR region (Dagamseh et al., 2008). Optimization of the front contact TCO has proven to be crucial for the high cell efficienty (Berginski et al., 2008).

Computer simulations for single junction a-Si:H PVC structure (Fig. 4) we compile in ASA software. The thicknesses of particular layers are show in Fig. 4. All important electric properties are set direct in the C-V characteristic for illuminated *p-i-n* PVC structure (Fig.6). Also in this case are the parameters I_{SC} and V_{OC} assigned from the graph, parameters *FF* and η are calculated by (eq. 1).
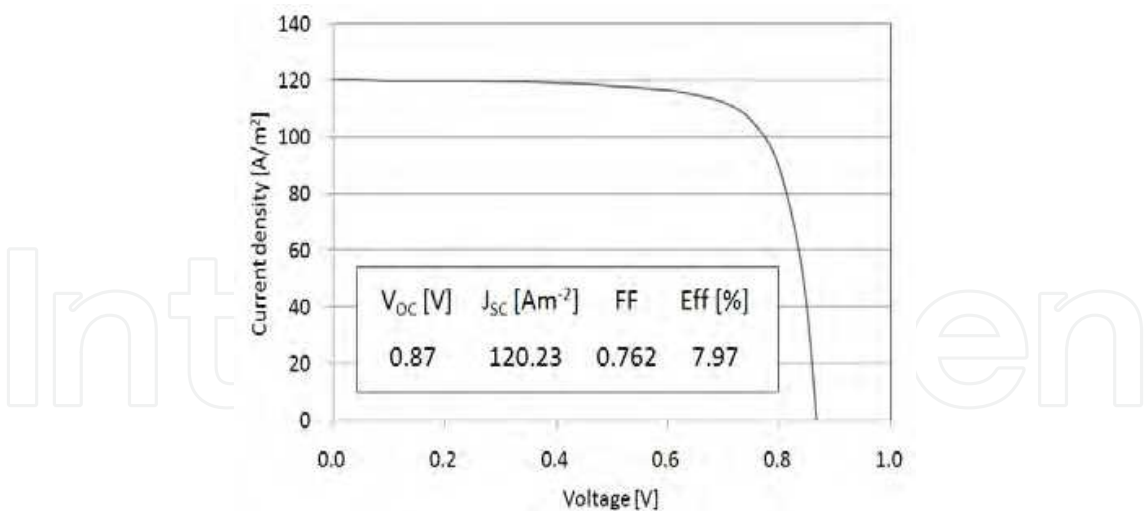
Fig. 6. C-V characteristics of TF PVC structure (illumination for AM1.5) for the thicknesses of ZnO:Al layer 800 nm and ZnO layer 100 nm

For the simulations the next parameters of TCO layers were used (obtained experimentally at the wavelength 500 nm):
1) ZnO:Al:
        - refractive index n = 2.675
        - absorption coefficient α = 1.71e5 m^{-1}

2) ZnO:
        - refractive index n = 2.052
        - absorption coefficient α = 7.55e5 m^{-1}

Reflection and quantum efficiency of selected thin film PVC structures for different thicknesses of ZnO layers a shown on Fig. 7 and Fig. 8.
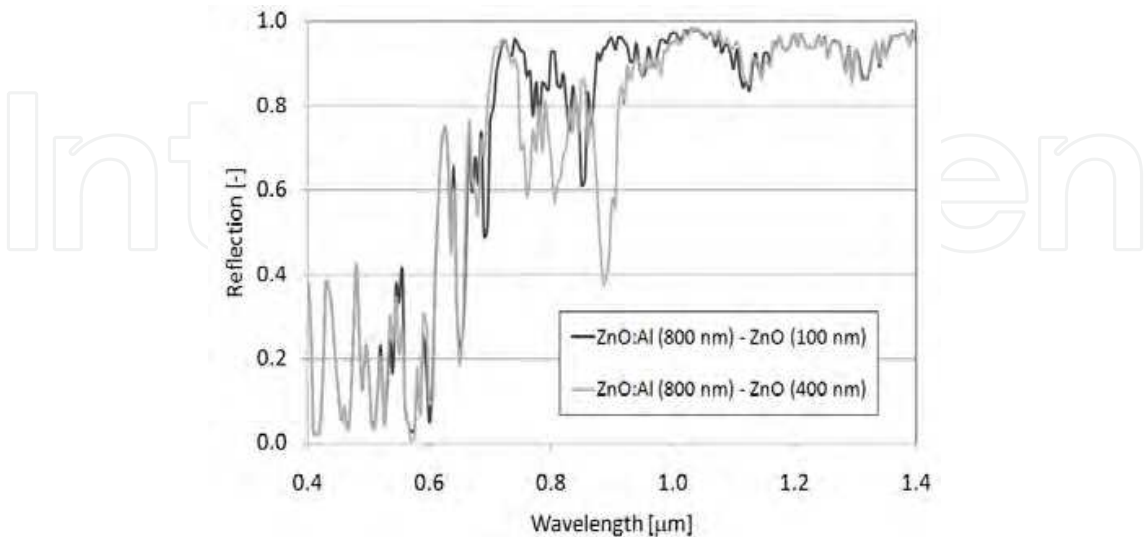
Fig. 7. Reflection of TF PVC structure for different thicknesses of ZnO layers
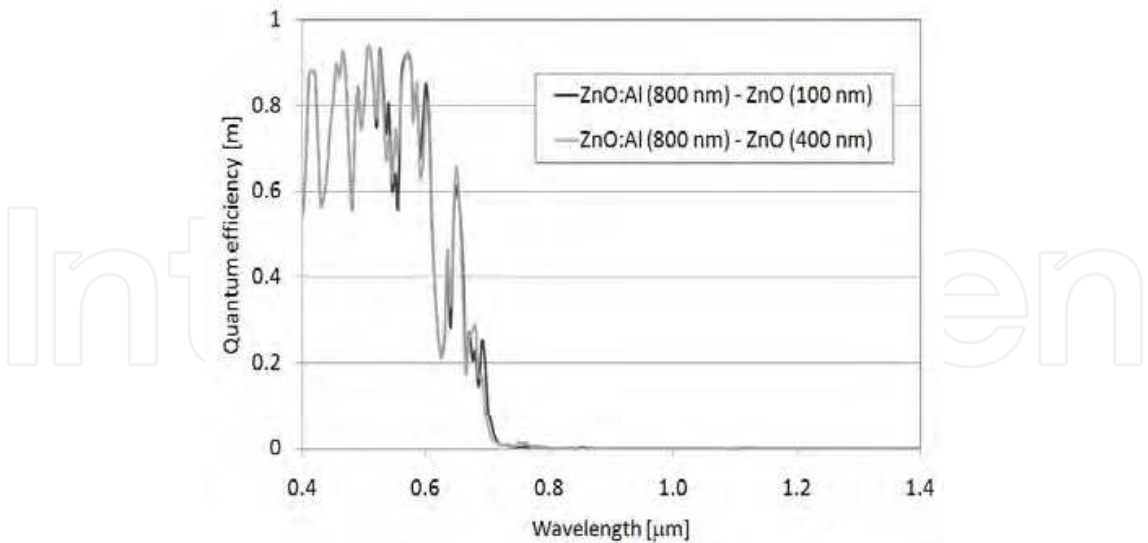
Fig. 8. Quantum efficiency of TF PVC structure for different thicknesses of ZnO layers

Reflection in the near IR region has a tendency to increase with the decrease of thickness of front ZnO layer. From dependences of quantum efficiency on wavelength result the fact, that the simple TF PVC structure shows lower effectiveness in the near IR region.

2.4 Sputtering

Computer simulations of magnetron sputtering corresponding to multi-source and multi-fold substrate rotation facilities have been progressively improved [Rother, 1999], [Jehn, 1999]. These calculations consider over-cosine distribution of sputter-deposited fluxes on the substrate area A_s, $dJ/dA_s \sim cos^n \Theta$, $1 < n \leq 2$, which reflects the kinetic energy losses of sputtered particles due to their collisions with working gas atoms.

We have applied the model and simulations of the spatial distribution of sputtered particles (Tvarozek et al., 1982) - deposition profile - in our diode system consisting of the plan-parallel arrangement of target and substrate in the distance of D (Fig. 9) with these idealized assumptions:

(a) Material of the target is emitted uniformly from the target area A_t;
(b) Angular distribution of the intensity of particles rejected from the target (sputtered particle flux J in the direction given by an angle Θ to the normal of surface) conforms with the Knudsen cosine law (Kaminsky, 1965)

$$J = J_0 \cos \Theta \tag{3}$$

or with its slight modifications, J_0 is the sputtered flux perpendicular to the target surface;
(c) Scattering of particles on the way to substrate is neglected;
(d) Accommodation coefficient of particles condensed on the substrate is equal 1 (re-sputtering is not included).

Then the flux of material sputtered from the target surface element dA_t to the substrate area element dA_s in the point P is given

$$d^2J = (J_0/\pi L^2)\, cos^2\,\Theta\, dA_t\, dA_s, \tag{4}$$

where Θ is an angle between $dA_t – dA_s$ path and the normal of target/substrate planes ($dA_t = dA_s\, cos\,\Theta$). By integrating of Eq. (4) over the target area A_t we can get the deposition profile $G(P)$ in the arbitrary point P on the substrate

$$G(P) = (\pi/J_0)\, dJ/dA_s = \int_{A_t} cos^2\,\Theta\, /L^2\, dA \tag{5}$$

It is useful to normalize the deposition profile $G_N(P)$ towards the maximal value of $G(0)$ which is usually the beginning of the co-ordinal system across the substrate

$$G_N(P) = G(P)\,/\,G(0) \tag{6}$$

For computing and simulations of deposition profiles we used Agilent Visual Engineering Environment (Agilent VEE Pro, 2009) - graphical language programming environment optimized for the use with electronic instruments, that provides a quick path to measurement and analysis.
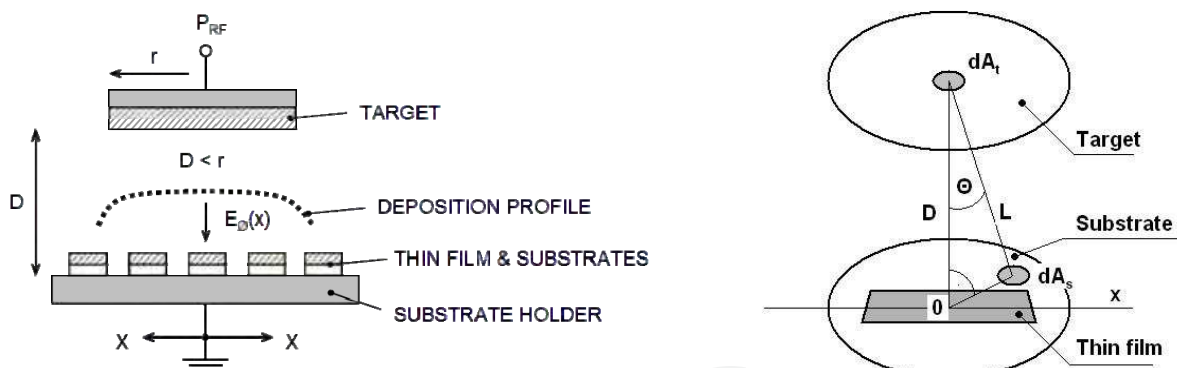

Fig. 9. Arrangement of the diode sputtering system

Simulated deposition profiles were compared with the lateral radial distribution of thin film thickness over the substrate. RF diode sputtering was performed at the working Ar gas pressure $p_{Ar} = 1.3$ Pa and Corning glass substrates were placed on different radial positions under the target of a diameter of 152.4 mm (ZnO+2 wt. % Al_2O_3) or of 76.2 mm (ZnO+2 wt. % Ga_2O_3 and ZnO+2 wt. % Sc_2O_3). In this case, simulations and experiments confirmed that an intensity of particles emitted from target approximately conforms to the Knudsen cosine law (Fig. 10 a). Changes of thin film thicknesses were less than 5% in the central substrate region of diameter $\leq$ ½ of target diameter. In lateral distances larger than target radius, the thin film thickness decreased down to 1/4 of the maximal value.

The detail comparison of various theoretical and experimental deposition profiles has shown that the sputtered fluxes from target follow slightly over-cosine angular distribution

during the diode sputtering at pressures below 1 Pa (Fig. 10 b). Sputtered particle flux J in the direction given by an angle Θ towards normal of target surface can be described by equation

$$J = J_0 \, (c_1 \cos \Theta + c_2 \cos^2 \Theta) \tag{7}$$

where the coefficients were estimated from experimental deposition profiles (approximately $c_2 \approx 0.1 \, c_1$).

Using the RF diode sputtering in the low-pressure region (p ≤ 1.3 Pa), the mean free path of sputtered particles (~ 10^{-2} m) is comparable with the distance of target – substrate and therefore we can assume "collision-less" regime, particularly for high energetic particles passed through RF discharge. Neutral sputtered particles and energetic species (ions neutralized at the target and reflected from it) sputtered from the target conform to the Knudsen cosine law slightly modified by over-cosine dependence and their spatial distribution on the substrate (deposition profile) is described by power cosine dependence (Eq. 5).
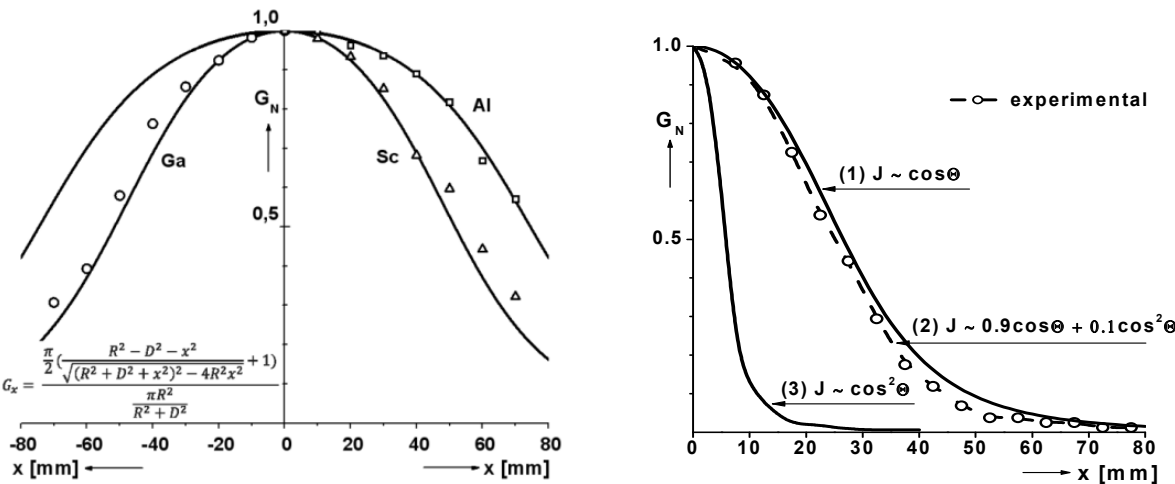

Fig. 10. Experimental and theoretical deposition profiles of: (a) ZnO:Al target with diameter of 152.4 mm and ZnO:Ga, ZnO:Sc targets with diameter of 76.2 mm; (b) target in diameter of 50.8 mm and comparison of deposition profiles calculated on the base of the Knudsen cosine law (curve 1) and the over-cosine angular dependence of sputtered particles (curves 2 and 3) with the experimental deposition profile

This "directional" sputtering can be exploited for preparation of strong textured thin films, e.g. c-axis inclined ZnO (Link, 2006) applicable in solar cells and in various optoelectronic devices, but also in an engineering of the nanoscale morphology, e.g. for preparation of a new class of optical nanomaterials – sculptured thin films – consisting of shaped, parallel, identical nanowires generally grown by physical vapor deposition techniques (Lakhtakia, 2008), (Jen, 2009).

3. Technology

We prepared ZnO:Al thin films in a planar RF sputtering diode system Perkin Elmer 2400/8L, using a ceramic target (ZnO+2 wt.% Al_2O_3) in Ar working gas at constant pressure of 1.3 Pa. Films with thickness from 560 nm to 800 nm, depended on the sputtering power density and deposition time, were deposited on Corning glass 7059 substrates. Three technology parameters (chosen to tailor the physical properties of the AZO films) were investigated: the sputtering RF power density E_Φ ($1.1 \div 4.4 \times 10^4$ W/m²), the substrate temperature T_s (RT, $100 \div 300°C$) and the post-deposition annealing at temperatures T_a ($200 \div 400°C$) in the forming gas (80% N_2 + 20% H_2) for 1 hour.

The real structure characterization (crystallite size and their crystallographic orientation, micro-strains and biaxial lattice stresses) of the films was investigated by X-ray diffraction (XRD) analysis. The XRD patterns were carried out using an automatic powder X-ray diffractometer AXS Bruker D8 equipped with a position sensitive area detector Histar. Cobalt Kα radiation (λ = 0.179 nm) was used as an X-rays source. Six strongest diffraction lines in the range of 2ϑ - diffraction angle from 30° to 80° of a ZnO powder are used as reference patterns. The position, height, integrated intensity and FWHM are the main four parameters that characterize the diffraction lines. The broadening of a diffraction line is a result of a real material structure, where the size of the crystallites and the micro-strains are the most important contributors to the broadening of the line. In this study we used a procedure utilizing an integral breadth of a diffraction line (Langford, 1978), (Delhez et al., 1982). Equation 8 characterizes the integral breadth β that includes two parameters namely the height and the integrated intensity:

$$\beta = \frac{I_{int}}{I_0} \tag{8}$$

where I_{int} is the integrated intensity (area below the line) and I_0 is the maximal intensity of the diffraction line. In general, the instrumental resolution of the equipment has also to be taken into account in order to obtain a physical (depended only on the properties of the matter) component of the broadening of the diffraction line. Furthermore, the physical component of the integral breadth of the diffraction line is a convolution of Cauchy and Gaussian components and so it is necessary to do de-convolution into a Cauchy part β_C^f and a Gaussian part β_G^f before the main real structure parameters are carried out. The Cauchy and Gaussian parts of the integral breadth of the line represent the size of the crystallites and the micro-strains, respectively. The average crystallite size and micro-strains are determined using Equations 9 and 10, respectively (Delhez et al., 1982):

$$<D> = \frac{\lambda}{\beta_C^f \cos\vartheta} \tag{9}$$

where <D> is the average crystallite size in the direction perpendicular to the diffracting lattice planes, λ is the X-ray wavelength used and ϑ is the Bragg's angle;

$$<\varepsilon> = \frac{\beta_G^f}{4\text{tg}\vartheta} \tag{10}$$

where $<\varepsilon>$ is the average micro-strain in the diffracting volume. Biaxial lattice stresses were calculated from a shift of the most intensive diffraction line (002) according to the equation (Sutta et al., 1982)

$$\sigma_1 + \sigma_2 = -\frac{E}{\mu} \cdot \frac{d - d_o}{d_o} \qquad (11)$$

where d_0 is the strain free reference lattice spacing, d is the lattice spacing obtained from the experiment, E is Young's modulus and μ is Poisson's ratio. Preferred orientation of crystallites (texture) in a certain direction can be approximately characterized by the Harris texture index (Okolo et al., 2005)

$$T_i = \frac{n \cdot I_i / R_i}{\sum_{j=1}^{n} I_j / R_j} \qquad (12)$$

where n is the number of investigated diffraction lines, I_i is the observed intensity and R_i is the corresponding intensity of the sample with randomly oriented crystallites (this value can be calculated from the theory if the structure of material is known or it can be picked up from the standard diffraction data files). In our case the R_i values were calculated from the theory. The maximal value that the Harris texture index can reach is equal to the number of lines taken into the calculation. For samples with completely randomly oriented crystallites the Harris texture index is equal to one.

The grain size was observed by transmission electron microscopy (TEM) by JOEL Electron Microscope. The thickness of AZO thin films was measured by DEKTAK 150, their electrical resistivity was obtained by Van der Pauw method and optical transmittance was determined by spectrometer Specord 210 and Avantes AVASPEC Fiber Optic Spectrometer.

The optical transmittance in the UV spectrum region (blue–shift of the absorption edge) gives the information about the width of optical band-gap. The absorption edge for direct inter-band transitions is given by

$$\alpha h v = A(h v - E_g)^{1/2} \qquad (13)$$

where A is a constant for a direct transition, a is the optical absorption coefficient, which is given from dividing absorbance by film thickness, and $h v$ is the photon energy. The direct band-gap of materials was obtained by plotting and extrapolation of $(\alpha h v)^2$ vs. $h v$.

4. Results and discussion

4.1 Deposition profile and properties of sputtered AZO thin films

AZO thin films were sputtered in the planar diode sputtering system (Fig. 9) at power density 4 times higher than the value of minimal energy flux density ($\sim 1 \times 10^4$ W/m^2). Corning glass substrates with dimension of 10x10 mm were placed on different positions under the target, ZnO+2 wt. % Al$_2$O$_3$, with diameter of 152 mm. We have applied the model of spatial distribution of sputtered particles in our diode system (see Section 2.4) to get continual changes of thickness of thin films in one deposition run from 700 nm in the center to 300 nm at the border of substrate holder (Fig. 10 a). All sputtered AZO films were

polycrystalline with the columnar structure and a very strong texture in the [001] direction perpendicular to the surface, what was confirmed by XRD, TEM and SEM analyses (Fig. 11, Fig.12). Properties of AZO thin films have been changed in lateral direction across the substrate holder. In the central region we can expect the highest power density (corresponding to deposition profile) what caused also an increase of mean grain size of 50 nm in comparison with value of 20 nm in peripheral position (Fig. 11 a).
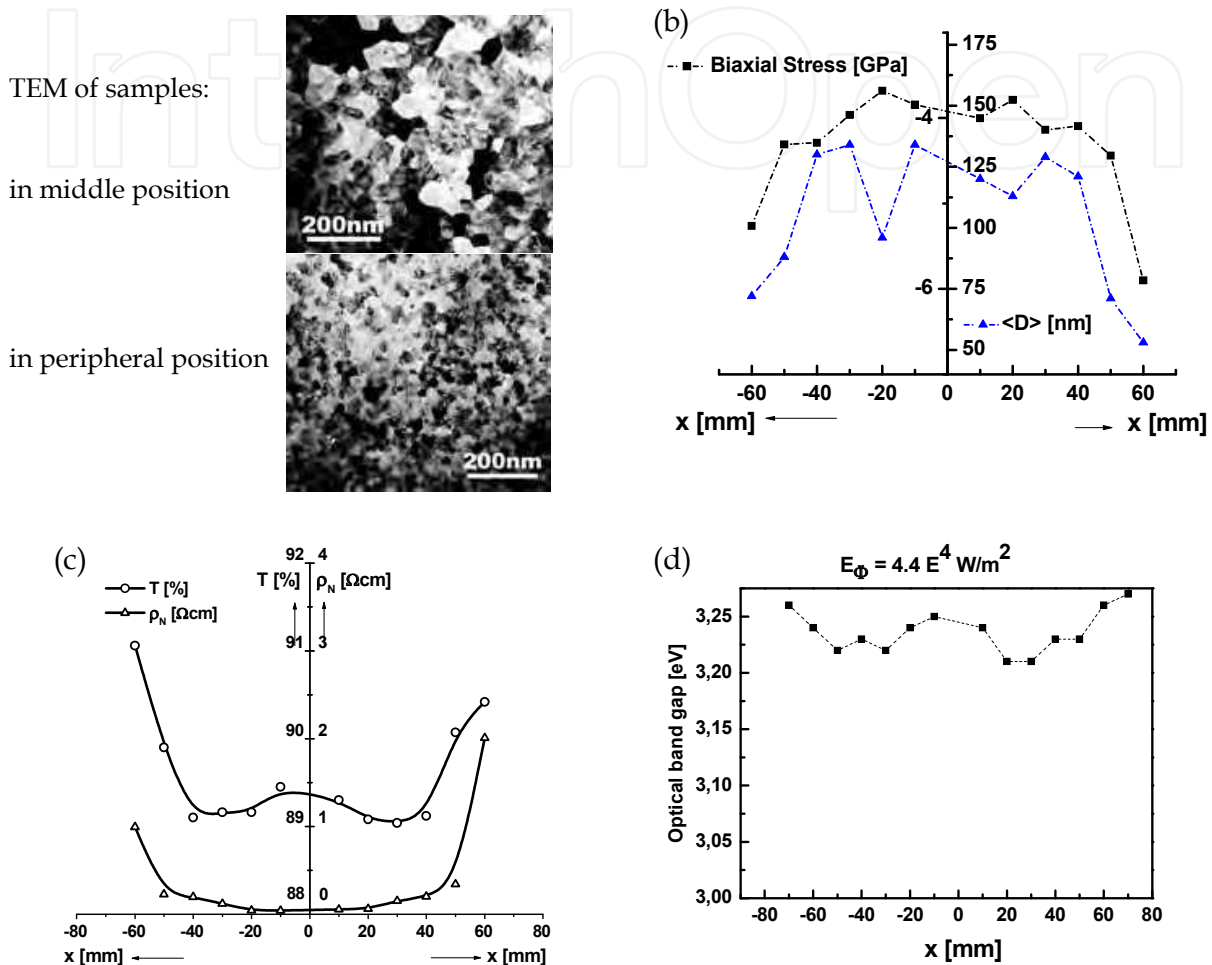

Fig. 11. Changes of properties of AZO thin films with the substrate position: (a) grain size observed by TEM, (b) lattice biaxial stresses $\sigma_1+\sigma_2$ and size of crystallites <D> evaluate from XRD patterns, (c) transmission T and resistivity ρ_N, (d) optical band gap E_{go}

Evaluation of XRD patterns also showed the tendency mentioned previously (Fig. 11 b): the average size of crystallites <D> (regions of coherent X-ray scattering) changed from 54 nm to 136 nm (in central region) and compressive lattice biaxial stresses $\sigma_1+\sigma_2$ increased from -3.8 GPa to -6.4 GPa (in peripheral position). Resistivity of AZO films placed in middle substrate region was in the range of 10^{-2} Ωcm and gradually towards the side of holder, has increased up to 3 Ωcm (Fig. 11 c). Remarkable increase of resistivity with position may be explained by the variation of particular fluxes of sputtered particles, dominantly by change of mutual ratios of sputtered ZnO, Al and O fluxes. Particularly, the bombardment of growing film by negative O ions generates large amount of oxygen intersticials that act as trap for free

electrons, thereby increasing the resistivity. Transmission of films sputtered in the central region was about 89 % and it increased to 91 % at the edge of substrate holder. The course of the optical band-gap dependence on substrate position is copying the transmittance dependence (Fig. 11 d).

For the explanation of previous mentioned phenomena, both effects the negative oxygen ion bombardment, or resputtering respectively, of growing film and the local atomic-scale heating of film surface by energetic secondary electrons, should be taken in the consideration. We assume, that it is a difference of the spatial distribution between energetic negative oxygen ions and secondary electrons, coming from the target and accelerating at it. Even the both fluxes have obtained the same kinetic energy (in order of 10 – 100 eV), the mean velocity of electrons and ions differs of 10^3-times because another masses. Therefore in the case of RF diode sputtering, the distribution of negative oxygen ions sputtered from the target will be more uniform across its area (in comparison with sputtered neutral particles) since the flux of negative oxygen ions is collimated by the induced electric field of target. The distribution of secondary electrons bombarding the growing film will follow the deposition profile because the induced target voltage has no significant influence on their angular emission due to small electron mass and high velocity. Then we can expect a higher local atomic-scale heating of the growing film in the central region.

We can conclude, that our arrangement provides sputtering of AZO thin films with relatively homogenous properties in the central region of diameter of 50 mm.

4.2 Influence of technological parameters on structural properties

Based on previous results we used the central region for sputtering and the effect of three technological parameters on structure of AZO thin films has been investigated: power density, substrate temperature and post-deposition annealing.

An increase of both sputtering power density up to $4,4.10^4$ W/m2 and substrate temperature to 200°C as well as post-deposition annealing provided highly textured films with a preferential c-axis [001] orientation (Fig. 13, 15, 17). Typical columnar structure of AZO films and their surface morphology are shown in Fig. 12.
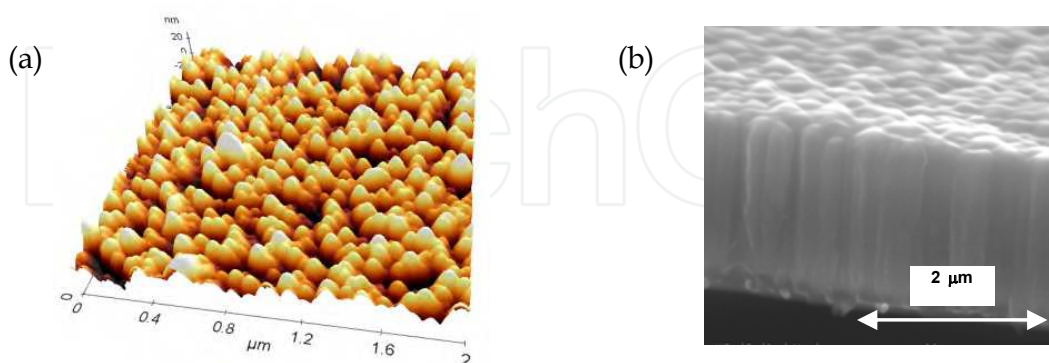

Fig. 12. The cross-section of typical polycrystalline AZO thin film with columnar structure in [001] direction perpendicular to the substrate and a hillock surface morphology

Significant asymmetry of (002) diffraction line when room substrate temperature was used indicates that there is a region with heterogeneous structure at the substrate – film interface (Fig. 13 a). Further energy delivered to the growing film by heating the substrate from RT to

200°C improved the crystallinity of the films (Fig. 15).The asymmetry of (002) line as well as heterogeneous regions completely diminished at higher substrate temperatures and small shifts from the reference line position were observed, which indicates only unimportant lattice strains (Fig. 15 b). The widths of (002) lines became narrower and dimensions of crystallites growing were from 60 to 120 nm for films deposited at RT and to more than 200 nm for those deposited at higher substrate temperatures. The widths of azimuthal line profiles also decreased from 15 to 3.5° with increasing energy delivered to the growing film during the deposition. This indicates lower declination of individual crystallites from the normal to the substrate (stronger texture). At the highest substrate temperature (300°C) also the other diffraction lines appeared, which is caused by more randomly oriented crystallites of the film. Other authors report the same changes with the temperature (Fu et al., 2003). In this case the film loosed its anisotropy. These phenomena induced by power density and temperature during deposition indirectly confirmed by changes of the surface morphology of films (Fig. 14, Fig. 16).
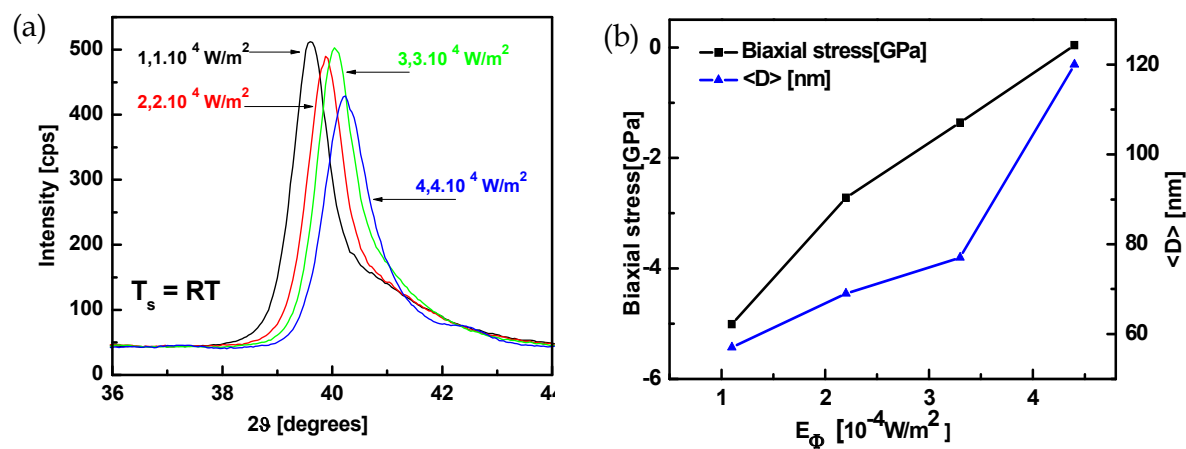
Fig. 13. AZO films sputtered at different power densities, $E_\Phi = 1{,}1 - 4{,}4.10^4\,W/m^2$: (a) XRD patterns, (b) dependences of biaxial lattice stress and crystallite size on power density
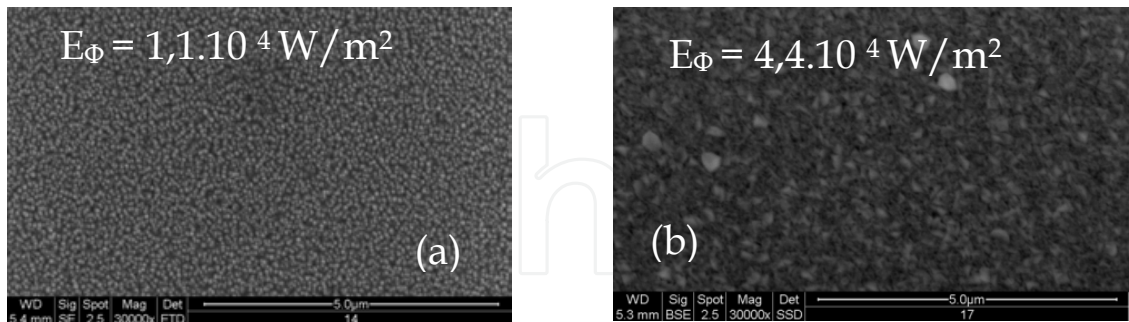

Fig. 14. Surface morphology of AZO films sputtered at different power densities: (a) $E_\Phi = 1{,}1.10^4\,W/m^2$, (b) $E_\Phi = 4{,}4.10^4\,W/m^2$

The shift up of the 2ϑ with increasing RF power, as well as substrate and annealing temperatures, is a result of the increase of Al^{3+} substituents (Al^{3+} that substitute for Zn^{2+} in the ZnO lattice) and a reduction of the interplanar distance, which changes the lattice distortion in AZO films from compressive to tensile lattice stresses. An increase of the power density and temperature during growth are resulting in the larger grains (growth from 60 to more than 200 nm) and better crystalline structure (no line asymmetry). In our

case the maximal value of the Harris texture index can reach the number 3 (3 lines of ZnO can be taken into the calculation in the range of $2\vartheta = 36 - 44°$). Value of $H_i = 2{,}97$ has confirmed the best crystallite texture (002) of films sputtered at the substrate temperature of 200 °C.
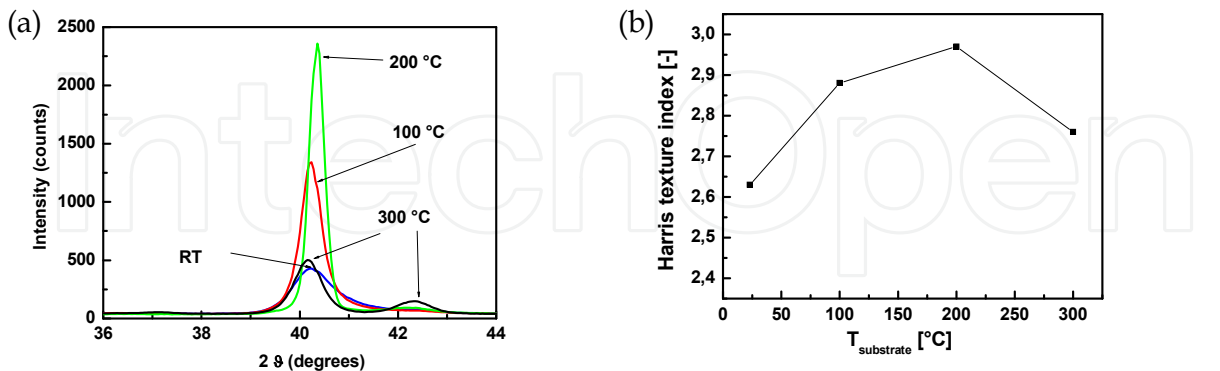
Fig. 15. AZO films sputtered at different substrate temperatures and constant power density, $E_\Phi = 4{,}4.10^4 \, \text{W/m}^2$: (a) RTG patterns, (b) Harris texture index
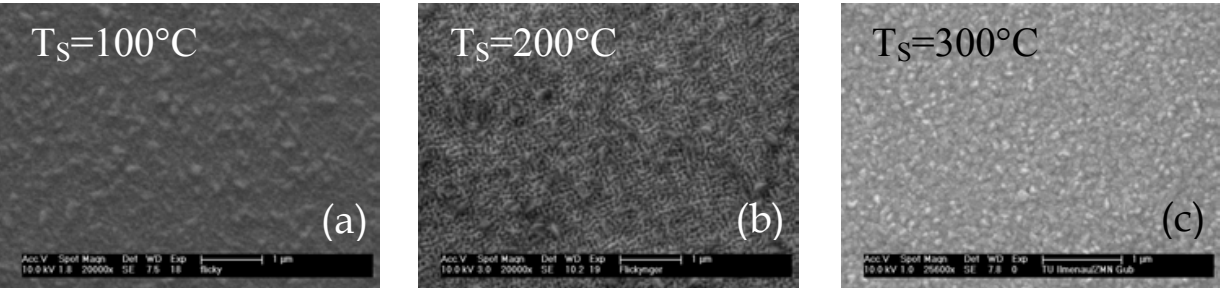
Fig. 16. Surface morphology of AZO films sputtered at different substrate temperatures T_S

Post-deposition annealing in the forming gas at 400 °C diminished an asymmetry of (002) diffraction line (Fig. 17).
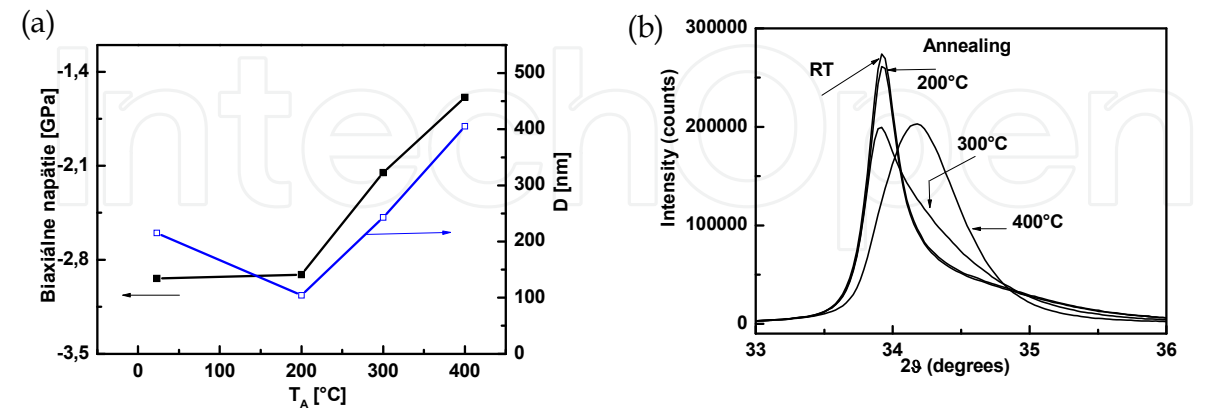
Fig. 17. Post-deposition annealing (in forming gas at T_A = 200 – 400 °C) of AZO films sputtered at room temperature of substrate and power density $E_\Phi = 4{,}4.10^4 \, \text{W/m}^2$: (a) RTG patterns, (b) dependences of biaxial lattice stress and crystallite size on annealing temperature

The average size of crystallites was ~ 100 nm at T_A = 200°C and it increased to ~ 400 nm by the growth of annealing temperature up to T_A = 400 °C (Fig. 17 b). Post-deposition annealing reduced biaxial lattice stresses due to elimination of grain boundary defects. Both effects can be explained by recrystallization and phase transformation.

4.3 Influence of technological parameters on electrical and optical properties

The substrate temperature increase during sputtering caused the decrease of sheet resistance from 300 Ω/square to 50 Ω/square with a minimum 36 Ω/square at T_s = 200°C (Fig. 18 a). Sputter power density has changed considerable R_s from 1137 Ω/square at E_Φ = 1.1.10^4 W/m^2 to 300 Ω/square at E_Φ = 4.4.10^4 W/m^2 (Fig. 18 b). After annealing (over the T_A > 200°C) the decrease of the sheet resistance to 10.4 Ω/square was observed (Fig. 18 c). The lowering of the sheet resistance by temperature (during or after deposition) was caused by both the improvement of crystalline structure and the increase of free electron concentration particularly, what has been supported by optical measurements.
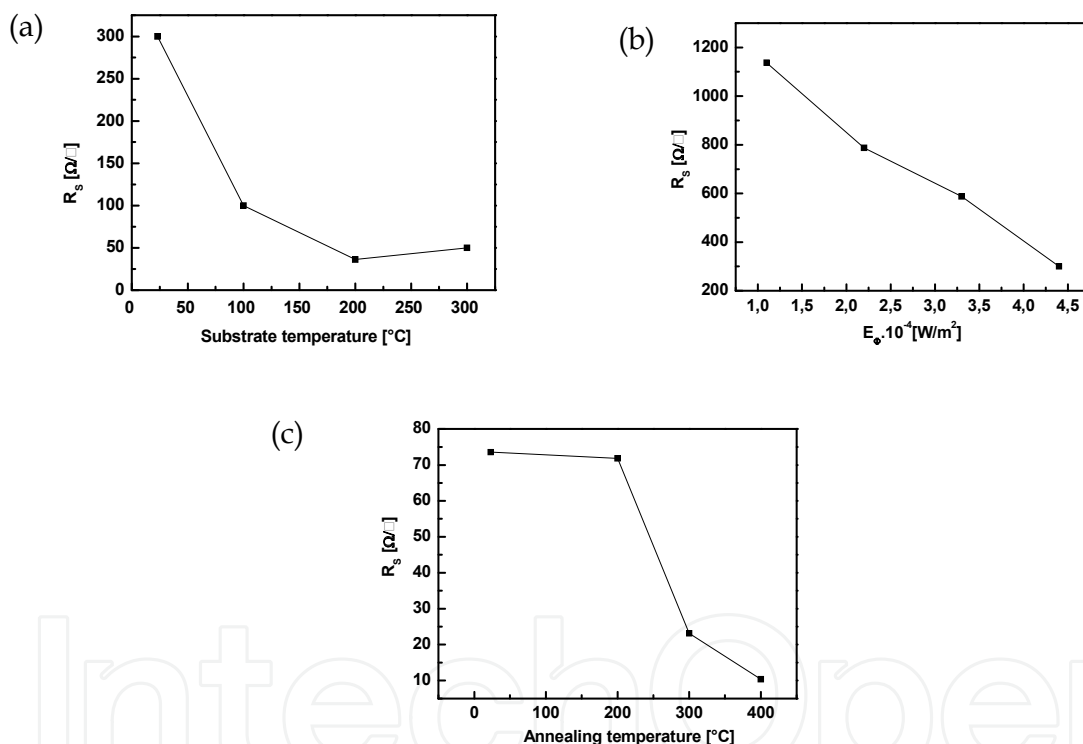

Fig. 18. The effect of: (a) substrate temperature, (b) power density and (c) annealing temperature on the sheet resistance

AZO thin films sputtered at a higher substrate temperature showed the "blue shift" in optical spectrum (Fig. 19), so-called the Burstein – Moss effect, which is dependent on the dopant concentration and the effective mass state density (Sernelius et al. 1988). The widening of the optical band-gap with the substrate temperature is originated by the increase of the electron concentration caused by Al doping (Liu et al. 2006), (Moon et al. 2006). No significant influence of the substrate temperature on the transmittance was observed (Fig. 20).
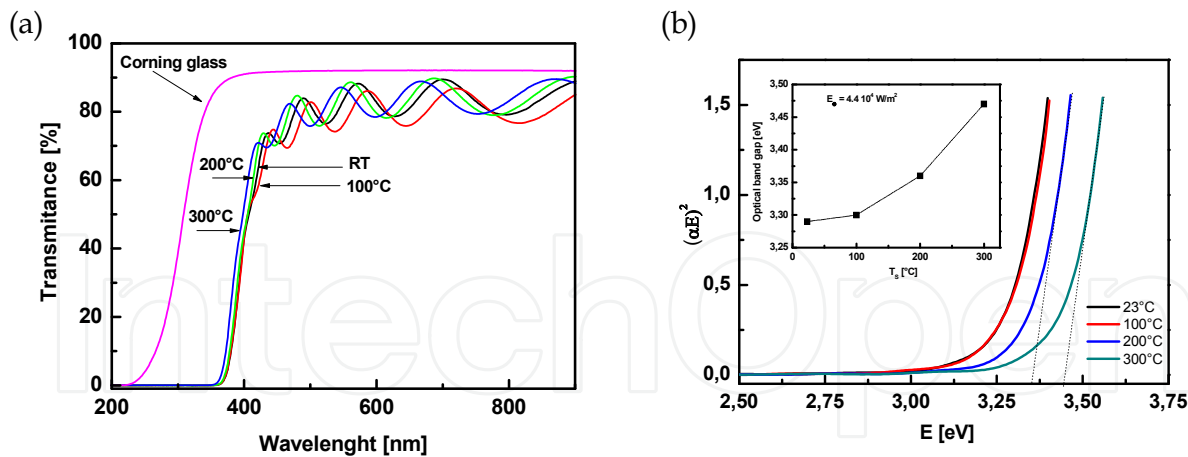
(a)

(b)

Fig. 19. The influence of the substrate temperature on: (a) the transmittance spectrum with glass substrate, (b) the blue–shift of the absorption edge and the optical band-gap width was obtained by plotting and extrapolation of $(\alpha h \nu)^2$ vs. $h \nu$.
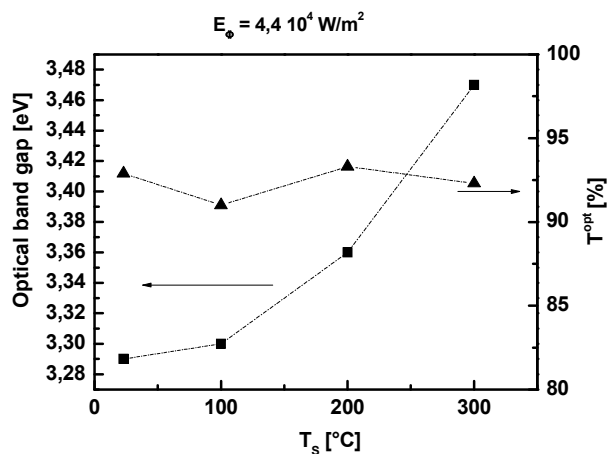

Fig. 20. The effect of the substrate temperature on the transmittance for AZO layer and the optical band-gap width

The dependence of transmittance on the power density showed a minimum at a middle powers and the highest value of 93 % was reached at power density of $E_\Phi = 4.4.10^4 \, W/m^2$ (Fig. 21). The post-deposition annealing had a positive effect on the increase of transmittance accompanied with the decrease of the optical band-gap width (Fig. 22).
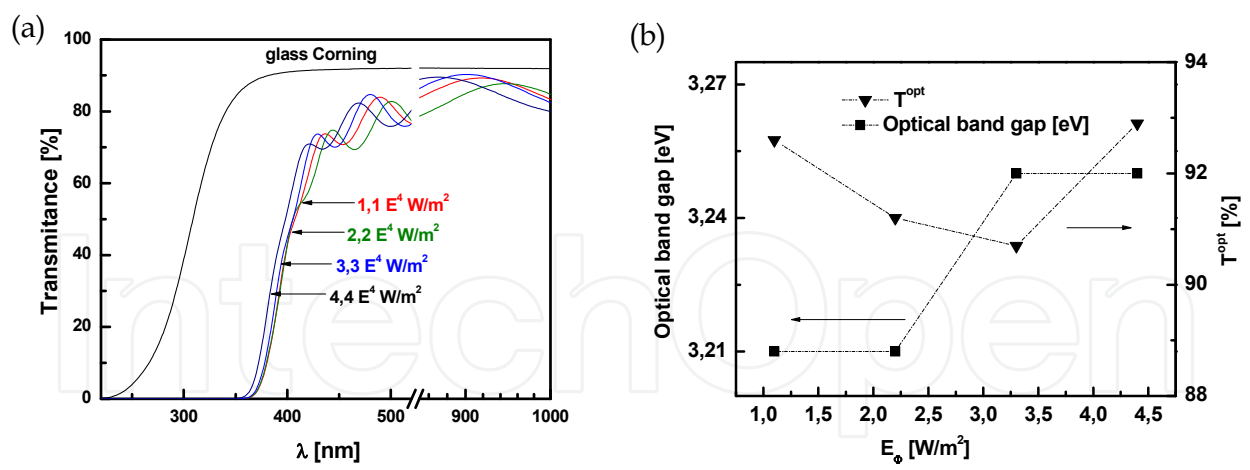
Fig. 21. The influence of the power density on: (a) the transmittance spectrum with glass substrate, (b) the transmittance only for AZO layer and the optical band-gap width
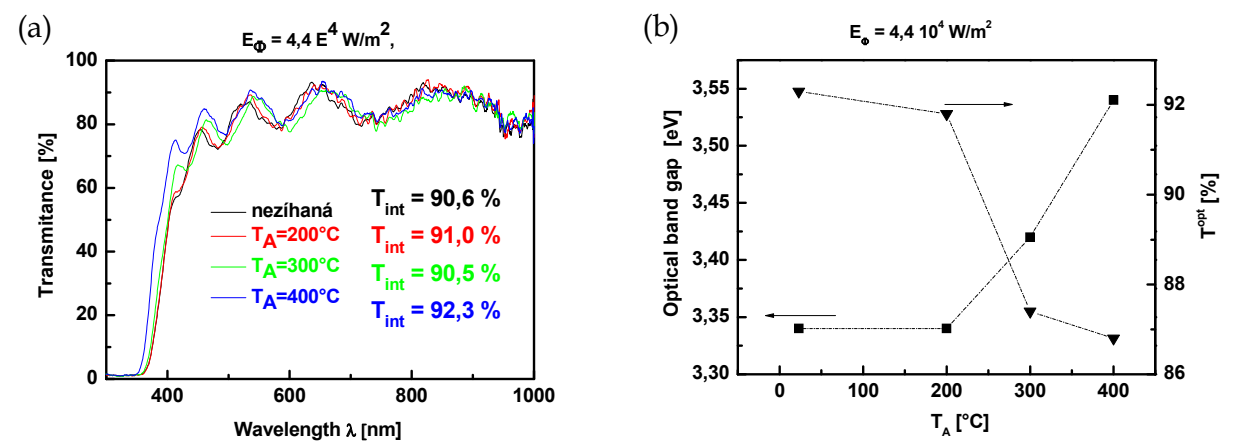

Fig. 22. The effect of the annealing temperature on: (a) the transmittance spectrum with glass substrate, (b) the transmittance only for AZO layer and the optical band-gap width

4.3 Summary

An influence of substrate temperature, power density, post-deposition annealing temperature on sheet resistance and transparency of sputtered AZO thin films are summarized in Table 1.

T_s [°C]	R_s [Ω]	T^{opt} [%]	$E_{\Phi} \cdot 10^{-4}$ [W/m²]	R_s [Ω]	T^{opt} [%]	T_A [°C]	T^{opt} [%]	R_s [Ω]
RT	300	92.9	1.1	1137	92.6	0	92.3	73.6
100	100	91.0	2.2	787	91.2	200	91.8	71.8
200	36	93.3	3.3	587	90.7	300	87.4	23.2
300	50	92.3	4.4	300	92.9	400	86.8	10.4

Tab. 1. The effect of substrate temperature T_s, power density E_{Φ}, post-deposition annealing temperature T_A on sheet resistance R_s and transmittance T^{opt} of sputtered AZO thin films

There is an inherent trade-off between how high transparent and low resistive TCO layer is, which is represented by the figure of merit: $F = T^{opt}/R_s$, where T^{opt} (%) is the transmittance for AZO layer and R_s (Ω/square) is the sheet resistance. The higher figure of merit ($F > 1\% / \Omega$) there is the better the performance of the TCO thin film. The substrate temperature increase during sputtering caused an improvement of the figure of merit to the value of $F = 2.6 \%/\Omega$ at 200 °C (Fig. 23 a). It showed a low value of $8 \times 10^{-2} \%/\Omega$ at the initial power density $E_\Phi = 1.1 \times 10^4 \text{ W/m}^2$ which became greater with growth of power density (Fig. 23 b). The greatest effect on the figure of merit exhibited the post-deposition annealing what increased of it up to value of $F = 8.9 \%/\Omega$ at $T_A = 400$ °C (Fig. 23 c).
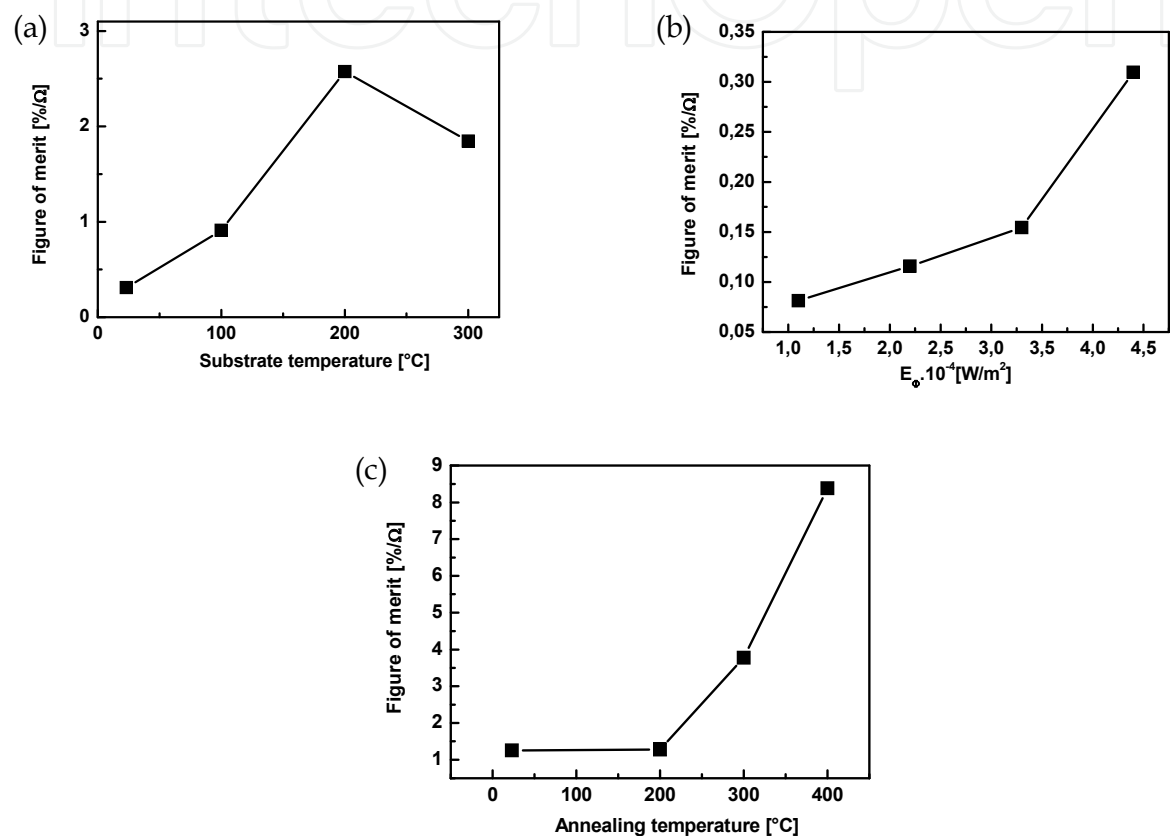

Fig. 23. Influence of substrate temperature (a), power density (b) and annealing temperature (c) on the figure of merit

5. Conclusion

AZO thin films sputtered at power density of $4.4 \times 10^4 \text{ W/m}^2$, substrate temperature of 200°C and annealed in the forming gas at 400°C showed a highly (002) oriented crystalline structure with the larger grains. Optimal substrate temperature could not surpass 200°C and on the other side, an annealing temperature should be higher than 200°C. Desired properties of AZO thin films for solar cell application - the high figure of merit ($F \geq 8 \%/\Omega$), low sheet resistance ($R_s \leq 10 \Omega$/square) and the highest transmittance ($T^{opt} \geq 86\%$) were obtained in highly oriented AZO films prepared at high values of power density, optimal substrate and annealing temperatures. The next experiments are focusing on the incorporation of AZO films into the real thin film solar cell, on the evaluation of their behaviour and on the

enhancement of light scattering by AZO film using chemical or ion etching modification of their surface.

6. Acknowledgments

7. References

Agilent VEE Pro, http://www.home.agilent.com/agilent/home.jspx, 2009

Ali, A. I. (2006). Growth and Characterization of ZnO:Al Thin Film Using RF Sputtering for Transparent Conducting Oxide, *Journal of the Korean Physical Society*, Vol., 49, (December 2006), pp. 652-656

Berginski, M.; Hupkes, J.; Reetz, W.; Rech, B. & Wuttig, M. (2008). Recent development on surface-textured ZnO:Al films prepared by sputtering for thin-film solar cell application, *Thin Solid Films*, Vol., 516, (October 2007), pp. 5836-5841

Dagamseh, A. M. K.; Vet, B.; Tichelaar, F. D.; Sutta, P. & Zeman, M. (2008). ZnO:Al films prepared by rf magnetron sputtering as back reflectors in thin-film silicon solar cells, *Thin Solid Films*, doi:10.1016/j.tsf2008.05.009

Delhez, R.; Keijser, T. H. & Mittemeijer (1982). Determination of crystallite size and lattice distortions through X-ray diffraction line profile analysis, *Fres. Z. Anal. Chem.*, Vol., 312, pp. 1-16

Fang G. J.; Li, D. & Yao, B. L. (2002). Influence of post-deposition annealing on the properties of transparent conductive nanocrystalline ZAO thin films prepared by RF magnetron sputtering with highly conductive ceramic target, *Thin Solid Films,* Vol., 418, pp. 156–162

Flickyngerova, S.; Netrvalova, M.; Prusakova L.; Novotny, I.; Sutta, P. & Tvarozek, V. (2009). Modification of AZO thin-film properties by annealing and ion etching, Vacuum, doi:10.1016/j.vacuum.2009.04.006

Fu E.G.; Zhuang D.M.; Zhang, G.; Yang, W. & Zhao, M. (2003). *Appl. Surf. Science*, Vol., 217, pp. 88-92

Fu E.G. & Zhuang D.M. (2004). Properties of transparent conductive ZnO:Al thin films prepared by magnetron sputtering, *Microelectronics Journal*, Vol., 35, pp. 383–387

Goetzberger, A. & Hoffmann, V.U. (2005). Photovoltaic Solar Energy Generation, Springer Verlag, 3-540-23676-7, Berlin

Jehn, H. A. & Rother, B. (1999). Homogeneity of multi-component PVD hard coatings deposited by multi-source arrangements, *Surface and Coatings Technology*, Vol., 112, pp. 103–107

Jen, Y-J.; Lakhtakia, A.; Yu, Ch-W. & Lin, Ch-T. (2009). Vapor-deposited thin films with negative real refractive index in the visible regime, *Optics Express*, Vol., 17, Issue 10, pp. 7784-7789, doi:10.1364/OE.17.007784

Kaminsky M. (1965). Atomic and ionic impact phenomena on metal surfaces, Springler Verlag, Berlin Heideberg

Kluth, O. & Rech: B (1999). Texture etched ZnO:Al coated glass substrates for silicon based thin Film cells, *Thin Solid Films*, Vol., 351, pp. 247-253

Kluth, O.; Schöpe, G.; Hüpkes, J.; Agashe, C.; Müller, J. & Rech B. (2003). Modified Thornton model for magnetron sputtered zinc oxide: film structure and etching behaviour, *Thin Solid Films*, Vol., 442, pp. 80–85

Lakhtakia, A.; Demirel, M.C.; Horn, M.W. & Xu, J. (2008). Six Emerging Directions in Sculptured Thin-Film Research, *Advances in Solid State Physics*, Vol., 46, pp. 295–307

Lim, D.G. & Kim D.H (2006). Improved electrical properties of ZnO:Al transparent conducting oxide films using a substrate bias, *Superlattices and Microstructures*, Vol., 39, pp. 107–114

Link, M.; Schreiter, M.; Weber, J.; Gabl, R.; Pitzer, D.; Primig, R. & Wersing W. (2006). c-axis inclined ZnO films for shear-wave transducers deposited by reactive sputtering using an additional blind, *J. Vac. Sci. Technol.*, Vol., A 24(2), pp. 218-222

Langford J. I. (1978). A rapid method for analyzing the breadths of diffraction and spectral lines using the Voigt function, *J. Appl. Cryst.*, Vol., **11,** pp. 10-14

Liu, Y.; Zhao, L. & Lian, J. (2006). Al-doped ZnO films by pulsed laser deposition at room temperature, Vacuum, Vol., 81, pp. 18–21

Ma H.L. & Hao, X. T. (2002). Bias voltage dependence of properties for ZnO:Al films deposited on flexible substrate, *Surface and Coatings Technology*, Vol., 161, pp. 58–61

Minami, T. (2005). Transparent Conducting oxide semiconductors for transparent electrodes, *Semicond. Sci. Technol.*, Vol., 20, pp. 35-44

Moon ,Y. K.; Kim, S. H. & Park J. W. (2006). The influence of substrate temperature on the properties of aluminum-doped zinc oxide thin films deposited by DC magnetron sputtering, *J Mater Sci: Mater Electron*, Vol., 17, pp. 973–977

Nelson, J. (2003). The Physics of Solar Cells, Imperial College Press, 1-86094-349-7, London

Oh, B. Y.; Jeong, M.Ch. & Myoung, J. M. (2007). Stabilization in electrical characteristics of hydrogen-annealed ZnO:Al films, *Applied Surface Science* Vol., 253, pp. 7157–7161

Okolo, B.; Lamparter, P.; Welzel, U.; Wagner, T.; Mittemeijer, E.J. (2005). The effect of deposition parameters and substrate surface condition on texture, morphology and stress in magnetron-sputter-deposited Cu thin films, *Thin Solid Films* Vol., 474, pp. 50– 63

Panjan, M.; Cekada, M.; Panjan, P.; Zalar, A. & Peterman, T. (2008). Sputtering simulation of multilayer coatings in industrial PVD system with three-fold rotation, *Vacuum*, Vol., 82, pp.158–161

PSpice A/D Circuit Simulator, http://www.ema-eda.com/products/orcad/pspice.aspx, 2009

Rieth, L. W. & Holloway, P. H. (2004). Influence. , J. Vac. Sci. Technol. A , Vol., 22 (No. 1), pp. 20-29

Rother, B.; Ebersbach, G. & Gabriel, H. M. (1999). Substrate-rotation systems and productivity of industrial PVD processes, *Surface and Coatings Technology*, Vol., 116– 119, pp. 694–698

Sernelius, B. E. (1988). Band gap tailoring of ZnO by means of heavy Al doping, *Physical Review* B, Vol., 37, number 17, pp. 10244-10248

Sittinger, V.; Ruske, F.; Werner W.; Szyszka B.; Rech, B.; Hupkes, J.; Schope, G. & Stiebig, H. (2006). ZnO:Al films deposited by in-line reactive AC magnetron sputtering for a-Si:H thin film solar cells, Thin Solid Films, 496, pp. 16 – 25

Sutta, P. & Jackuliak, Q. (1998). Macro-stress Formation in Thin Films and its Determination by X-ray Diffraction, In: Proc. of the 2nd International Conference on Advanced Semiconductor Devices and Microsystems, *ASDAM'98*, pp. 227-230

Thorton, J. A. & Hoffman, D. W. (1989). Stress-related effects in thin films, *Thin Solid Films*, Vol., 171, pp. 5-31

Tominaga, K.; Iwamura, S.; Shintani Y. & Tada, O. (1982). Energy Analysis of high – energy Neutral Atoms in the Sputtering of ZnO and BaTiO3, Jpn. J. Appl. Phys., Vol., 21, (No. 5), pp. 688-695

Tvarozek, V.; Harman, R. & Jesenakova, V. (1982). Simultaneous sputtering of several materials from composite target, *Jemna mechanika a optika*, Vol. XXVII, No. 4, pp. 89-94

Tvarozek, V.; Novotny, I.; Sutta, P.; Flickyngerova, S.; Shtereva K. & Vavrinsky E. (2007). Influence of sputtering parameters on crystalline structure of ZnO thin films, *Thin Solid Films*, Vol., 515, pp. 8756-8760

Zeman, M. (2007). Advanced Amorphous Silicon Solar Cell Technolgies, In: *Thin film solar cells: fabrication, characterization and applications*, Poortmans, J. & Arkhipov, V., pp. 173-236, John Wiley & Sons, 978-0-470-09126-5, New York

Zeman, M.; Van den Heuvel, J.; Kroon, M.; Willemen, J.; Pieters, B. & Krč, J. (2005). ASA, Users Manual,Version 5.0, Delft University of Technology, The Netherlands

Semiconductor Technologies

Edited by Jan Grym

Semiconductor technologies continue to evolve and amaze us. New materials, new structures, new manufacturing tools, and new advancements in modelling and simulation form a breeding ground for novel high performance electronic and photonic devices. This book covers all aspects of semiconductor technology concerning materials, technological processes, and devices, including their modelling, design, integration, and manufacturing.

How to reference

In order to correctly reference this scholarly work, feel free to copy and paste the following:

Vladimir Tvarozek, Pavol Sutta, Sona Flickyngerova, Ivan Novotny, Pavol Gaspierik, Marie Netrvalova and Erik Vavrinsky (2010). Preparation of Transparent Conductive AZO Thin Films for Solar Cells, Semiconductor Technologies, Jan Grym (Ed.), ISBN: 978-953-307-080-3, InTech, Available from: http://www.intechopen.com/books/semiconductor-technologies/preparation-of-transparent-conductive-azo-thin-films-for-solar-cells

INTECH
open science | open minds